Research Square

Preprints are preliminary reports that have not undergone peer review.
They should not be considered conclusive, used to inform clinical practice,
or referenced by the media as validated information.

Reversing Optical Energy Dissipation in Ultrathin MoS_2 Cavities at Telecommunication Wavelengths

Jialin Liu
Institute of Materials Research and Engineering, Agency for Science, Technology and Research, 2 Fusionopolis Way, Singapore 138634, Singapore

Haoyu Ge
Institute of Materials Research and Engineering, Agency for Science, Technology and Research, 2 Fusionopolis Way, Singapore 138634, Singapore.

Yingshu Yang
National Key Laboratory of Shock Wave and Detonation Physics, Institute of Fluid Physics, China Academy of Engineering Physics, Mianyang, 621900, China

Matej Sebek
Institute of Materials Research and Engineering, Agency for Science, Technology and Research, 2 Fusionopolis Way, Singapore 138634, Singapore

Gang Wu
Institute of Advanced Intelligence and Computing (IAIC), Agency for Science, Technology and Research, 1 Fusionopolis Way, Singapore 138632, Singapore

Qing Yang Steve Wu
Institute of Materials Research and Engineering, Agency for Science, Technology and Research, 2 Fusionopolis Way, Singapore 138634, Singapore

Chee Leng Lay
Institute of Materials Research and Engineering, Agency for Science, Technology and Research, 2 Fusionopolis Way, Singapore 138634, Singapore.

Eugene Jia Hao Soh
Institute of Materials Research and Engineering, Agency for Science, Technology and Research, 2 Fusionopolis Way, Singapore 138634, Singapore.

Ai Jia Sim
Institute of Materials Research and Engineering, Agency for Science, Technology and Research, 2 Fusionopolis Way, Singapore 138634, Singapore.

Kandammathe Valiyaveedu Sreekanth
Institute of Materials Research and Engineering, Agency for Science, Technology and Research, 2 Fusionopolis Way, Singapore 138634, Singapore.

Jinghua Teng
TENG_Jing_Hua@a-star.edu.sg

Institute of Materials Research and Engineering, Agency for Science, Technology and Research, 2 Fusionopolis Way, Singapore 138634, Singapore.

Zeng Wang

wang_zeng@a-star.edu.sg

Institute of Materials Research and Engineering, Agency for Science, Technology and Research, 2 Fusionopolis Way, Singapore 138634, Singapore.

Research Article

Keywords: Standing-wave engineering, Optical energy dissipation, Target-layer absorption, Molybdenum disulfide, Ga-ion implantation, Ultrathin optical cavities

Posted Date: November 10th, 2026

DOI: https://doi.org/10.21203/rs.3.rs-11664696/v1

License: This work is licensed under a Creative Commons Attribution 4.0 International License. Read Full License

Additional Declarations: The authors declare no competing interests.

Reversing Optical Energy Dissipation in Ultrathin MoS_2 Cavities at Telecommunication Wavelengths

Jialin Liu[1], Haoyu Ge[1], Yingshu Yang[3], Matej Sebek[1], Gang Wu[2], Qing Yang Steve Wu[1], Chee Leng Lay[1], Eugene Jia Hao Soh[1], Ai Jia Sim[1], Kandammathe Valiyaveedu Sreekanth[1], Jinghua Teng[*1], and Zeng Wang[*1]

[1]Institute of Materials Research and Engineering, Agency for Science, Technology and Research, 2 Fusionopolis Way, Singapore 138634, Singapore.

[2]Institute of Advanced Intelligence and Computing (IAIC), Agency for Science, Technology and Research, 1 Fusionopolis Way, Singapore 138632, Singapore.

[3]National Key Laboratory of Shock Wave and Detonation Physics, Institute of Fluid Physics, China Academy of Engineering Physics, Mianyang, 621900, China.

Correspondence:

Zeng Wang email: wang_zeng@a-star.edu.sg
Jinghua Teng email: jh-teng@a-star.edu.sg

Abstract

Planar optical cavities are widely used to enhance light–matter interactions in ultrathin materials, and are readily integrated into on-chip devices. While cavity designs commonly focus on suppressing reflection, low reflectance alone does not reveal where the incident optical energy is ultimately dissipated. In metal-backed cavities, absorption can occur either in the functional target layer or parasitically in the metallic reflector, leading to a fundamental competition that is particularly detrimental for weakly absorbing ultrathin semiconductors. Here, we demonstrate that the dominant optical dissipation channel in planar cavities can be reversed through the combined control of standing-wave field overlap and target-material loss. Using a layer-resolved electromagnetic model, we show that positioning a standing-wave antinode within the target layer strengthens its absorption relative to that of the metallic reflector, enabling efficient redirection of optical energy into the functional material. Using a model system comprising molybdenum disulfide (MoS_2), aluminum oxide (Al_2O_3), and aluminum (Al) operating at telecommunication wavelengths, we introduce gallium (Ga) ion implantation to systematically modify the optical loss of MoS_2. Together, dielectric-spacer engineering and controlled loss modification enable a transition from reflector-dominated to target-dominated absorption, with the MoS_2 layer capturing up to 72% of the incident power in a structure only about $\lambda/10$ thick. For pristine MoS_2, the maximum calculated cavity-induced absorption enhancement exceeds tenfold relative to a MoS_2/quartz reference at the same wavelength. These findings establish standing-wave field overlap and material loss as two key parameters jointly governing where optical energy is dissipated, providing a general

framework for directing optical energy into functional materials while minimizing parasitic metal losses.

Keywords: Standing-wave engineering, Optical energy dissipation, Target-layer absorption, Molybdenum disulfide, Ga-ion implantation, Ultrathin optical cavities.

Introduction

Ultrathin semiconductors are attractive building blocks for compact on-chip photodetectors and modulators. However, their nanometer-scale thickness results in inherently weak light absorption, particularly in technologically important near-infrared telecommunication bands, where many semiconducting van der Waals (vdW) materials become nearly transparent. [1-3] Enhancing light–matter interactions in such ultrathin films is therefore central to compact optical devices and emerging on-chip photonics. [4] Owing to their tunable optical and optoelectronic responses, vdW materials offer a versatile platform for reconfigurable metaoptics, electrically controlled excitonic devices, and tunable photodetection. [5-7] Realizing the full potential of these materials, however, requires strategies that not only increase total absorption but also ensure that optical energy is deposited within the functional material itself. Metal-backed planar cavities offer an attractive fabrication-friendly approach for enhancing optical interactions without requiring complex in-plane nanopatterning. [8-10] Their design is often framed in terms of anti-reflection concepts, whereby destructive interference suppresses reflection and increases the total absorption of the structure. [8,9,11] However, low reflectance does not necessarily imply efficient excitation of the target layer. The absorbed optical energy may be dissipated in the functional layer, within the metallic backplane, or distributed between the two. [9,10,12] Consequently, cavities exhibiting similar reflectance spectra may possess different energy-dissipation pathways. Figure 1 illustrates the complementary roles of reflection suppression, standing-wave field overlap, and layer-resolved absorption. Destructive interference reduces the net reflected field (Figure 1a), whereas cavity design controls the internal field distribution and its overlap with the target

layer (Figure 1b). The resulting absorption partition depends on both this field distribution and the optical loss of each constituent material (Figure 1c). Controlling these coupled factors is therefore essential to directing optical energy into the functional layer.

The complexity arises because the metallic reflector participates in both optical confinement and energy dissipation. Unlike an ideal perfect electric conductor, a real metal has a finite complex refractive index that determines the amplitude and phase of reflection while permitting field penetration and absorption. [13] The standing-wave node is therefore displaced into the metal rather than being pinned at its surface, causing a non-negligible fraction of the optical energy to be dissipated in the reflector itself. [13,14] The field established by the complete multilayer structure drives absorption in both the target layer and the metal, creating competition between the useful and parasitic absorption channels. [15] This competition is particularly consequential for ultrathin, weakly absorbing vdW materials, whose limited dissipation can leave the reflector as the principal sink for optical energy, even when the cavity exhibits a strong absorption resonance. [9,12]

Here, we show that optical energy dissipation in ultrathin planar cavities can be engineered and even reversed through deliberate cavity design and material-loss control. Using $MoS_2/Al_2O_3/Al$ cavities as a model platform, where pristine MoS_2 is weakly absorbing over the investigated near-infrared spectral range, we demonstrate that standing-wave engineering enhances MoS_2 target-layer absorption by up to 11.25-fold relative to the MoS_2/quartz reference at the same wavelength. A layer-resolved electromagnetic model identifies two

coupled factors governing the dissipation balance: the internal field overlap and the material optical loss. To experimentally probe their interplay, we systematically tune the optical loss of MoS_2 through Ga-ion implantation. Using optical constants fitted to measured reflectance spectra, the model reveals a transition from metal-dominated to MoS_2-dominated absorption, with up to 72% of the incident power absorbed within the MoS_2 layer in a cavity with a total thickness of approximately λ/10. These findings establish a general strategy for controlling optical dissipation pathways in ultrathin photonic structures by coordinating standing-wave field overlap and material loss.

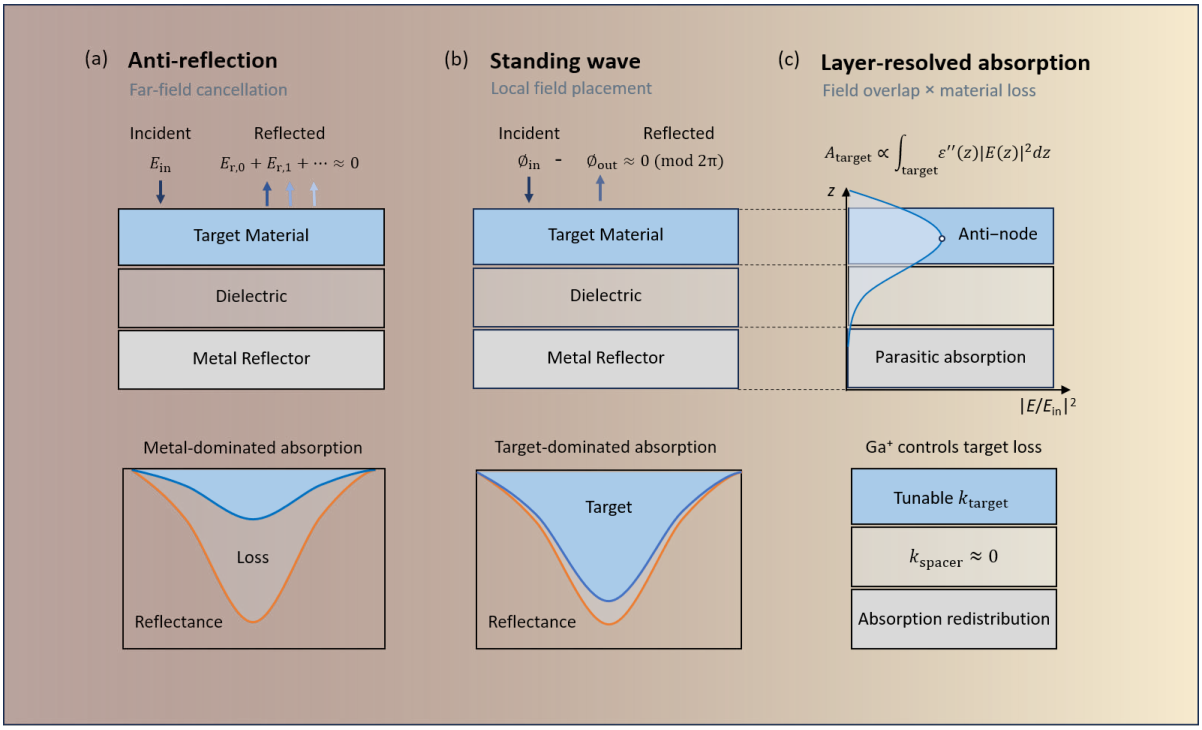


Figure 1. Reflection suppression, standing-wave field overlap, and absorption partition in metal-backed optical cavities. (a) Destructive interference between reflected contributions suppresses the net reflection, but does not determine how the absorbed power is partitioned between the target layer and the metallic reflector. (b) Standing-wave engineering controls the overlap of the internal electric field with the target layer. The phase relation schematically indicates approximately in-phase incident and reflected fields at a common reference plane. The lower diagrams in (a,b) illustrate different partitions of incident power into reflection, target-layer absorption, and parasitic metal absorption under negligible transmission. (c) Target-layer absorptance is governed by the field intensity integrated over the target layer and weighted by the local dielectric loss, ε''. The field profile illustrates overlap with an antinode and finite penetration

into the metallic reflector. With a nearly lossless spacer, tuning the target-layer optical loss together with the field distribution enables a transition from metal-dominated to target-dominated absorption. All field profiles and spectral diagrams are schematic.

Results

1. Standing-Wave Control of Absorption in Ultrathin MoS_2

To connect the optical response of the cavity with absorption in its constituent layers, we analyze the planar multilayer structure using the transfer matrix method with Poynting flux analysis (TMM-PFA). [15,16] The cavity is modeled as a planar stack consisting of a target layer of thickness d_t and complex refractive index $\tilde{n}_t = n_t + ik_t$, separated from a metallic reflector $\tilde{n}_r = n_r + ik_r$ by a lossless dielectric spacer of thickness d_s and refractive index n_s. Air refractive index n_0, serves as the incident medium.

The multilayer solution accounts for propagation and multiple reflections, providing the reflectance and the internal electric field distribution. [15,17] Layer-resolved absorptance is obtained directly from the Poynting-flux difference across each layer's boundaries, normalized to the incident flux. [16,18] This approach enables independent evaluation of absorption within the target layer and metal reflector, therefore determining whether a reduction in reflectance is accompanied by enhanced absorption in the target layer. Details of the TMM formulation and the Poynting-flux calculation of layer-resolved absorptance are provided in Supplementary Information Section 1.

By the time-averaged Poynting theorem, the net power flux entering a layer equals the power dissipated within it. [13,15] For a nonmagnetic planar structure at normal incidence, the target-layer absorptance can be written equivalently as:

$$A_{\mathrm{a}}(\lambda) = \frac{\omega \varepsilon_0}{2 I_{\mathrm{inc}}} \int_{\mathrm{target}} \varepsilon_{\mathrm{a}}''(\lambda) |E(z,\lambda)|^2 \, \mathrm{d}z \qquad (1)$$

where I_{inc} is the incident intensity, ω is the angular frequency, ε_0 is the vacuum permittivity, $\varepsilon_a{}''$ is the imaginary part of the target-layer relative permittivity, and $E(z,\lambda)$ is the complex electric-field amplitude within the structure. Equation (1) provides the quantitative basis for the layer-resolved absorption picture in Figure 1c: target-layer absorptance is governed by the overlap of the internal field intensity with the material's dielectric loss. For a homogeneous target layer, the loss weight is $\varepsilon_a{}'' = 2n_t k_t$, while the field distribution depends on the optical constants and geometry of the complete stack. The spacer thickness and the metal's complex reflection coefficient influence this integral by modifying the internal field, while the target-layer optical constants determine both its dissipative response and its contribution to the multilayer interference. A field maximum within the target layer therefore favors absorption but does not alone establish either strong target-layer absorptance or a small metal-loss fraction. Both must be evaluated from the dissipation in the complete structure. Further details of the TMM-PFA layer-resolved absorption calculation and the cavity–reference comparison are provided in Supplementary Information Section 1 and Figure S1.

We demonstrate the above design concept in the near-infrared using a planar $MoS_2/Al_2O_3/Al$ three-layer structure, as shown in Figure 2b. Pristine MoS_2 exhibits weak absorption in the investigated near-infrared range, consistent with the measurements of the no-cavity MoS_2/quartz reference (Supplementary Information Section 2 and Figure S2). The mechanically exfoliated MoS_2 (~40 nm thick) was transferred onto the Al_2O_3 dielectric spacer deposited on an Al-coated quartz substrate to construct the optical cavity. Atomic force

microscopy (AFM) characterization of the transferred flakes is provided in Supplementary Information Section 3 and Figure S3. The 50-nm-thick Al layer serves not only as a highly reflective mirror that provides strong optical feedback but also as a source of non-trivial interfacial phase shift that strongly influences the cavity standing-wave distribution. To examine the influence of reflector selection, Figure 2a maps the calculated absorptance as a function of the reflector's refractive index and extinction coefficient, with Al, gold (Au) and chromium (Cr) marked as representative metals. The maps compare the dielectric/metal structure with and without the MoS_2 target layer. With the dielectric spacer and substrate treated as lossless, absorption in the structure without MoS_2 arises entirely from the metal. After MoS_2 is introduced, the plotted total absorptance consists of contributions from both the target layer and the reflector. Introducing MoS_2 changes the internal field distribution and alters absorption in the Al reflector. The difference in total absorptance between the two structures cannot generally be assigned solely to MoS_2. The MoS_2 contribution must instead be evaluated separately within the complete cavity. To directly visualize the standing-wave field distribution in the cavity and to cross-check the TMM results, finite-difference time-domain (FDTD) full-wave simulations were performed for the same cavity (Supplementary Information Section 4 and Figure S4). Figure 2b shows the wavelength-dependent field distribution and a corresponding cross-sectional profile along the z direction. The profile shows the MoS_2 layer is near an electric-field antinode, with a lower field amplitude towards the metal interface. This spatial overlap supports the field-enhancement mechanism of the cavity: through the loss-weighted field integral in Equation (1), the enhanced field within MoS_2 is converted directly into the layer-resolved absorptance. The spacer thickness sets the

propagation phase that positions this antinode and therefore determines how strongly the field overlaps the MoS_2 layer.

Increasing the Al_2O_3 spacer thickness from 45 to 65 and 95 nm redshifts the calculated reflectance minima (Figure 2d). To experimentally verify the spacer-dependent optical response, we fabricated three sets of samples with the corresponding Al_2O_3 thicknesses and measured their reflectance using Fourier transform infrared spectroscopy (FTIR), as shown in Figure 2e. The measured spectra reproduce the redshift, with reflectance minima at approximately 1420, 1700 and 1950 nm, respectively. Consistent with the standing-wave interpretation, the calculated zero crossings of the reflection phase of the complete cavity also shift towards longer wavelengths and closely coincide with the measured reflectance minima (Figures 2d, e). Small discrepancies between the calculated and measured spectral positions may arise from variations in MoS_2 thickness or optical properties among individual flakes. To determine whether the cavity response enhances absorption in the target material itself, we evaluate the layer-resolved absorptance. As shown in Figure 2c, the calculated peak absorptance of MoS_2 is enhanced by factors of 8.40, 7.32 and 11.25 for the cavities with 45-, 65- and 95-nm Al_2O_3 spacers, respectively, relative to the corresponding no-cavity MoS_2/quartz references evaluated at the same wavelengths (Supplementary Information Section 5, Figure S5 and Table S1). The corresponding MoS_2 peak absorptances are approximately 4.50%, 3.25% and 2.39%, occurring at $\lambda_{MoS_2}^{peak} \approx$1360, 1550, and 1820 nm, respectively (denoted λ_{peak} hereafter). Notably, the wavelengths of the MoS_2 absorptance maxima need not coincide with those of the reflectance minima. When transmission is negligible, the reflectance minima correspond to the maxima in total absorptance, whereas the

maxima of MoS_2 absorptance depend on dissipation within MoS_2 alone. Differences from the measured reflectance minima can additionally reflect the simulation–experiment offsets discussed above. Thus, these results establish that standing-wave engineering can selectively redirect optical dissipation toward the target MoS_2 layer itself. Despite the substantial relative enhancement, the absolute absorptance of pristine MoS_2 remains low, motivating further investigation of how target-material loss influences both absorption within MoS_2 and the partition of absorbed power between MoS_2 and the Al reflector.

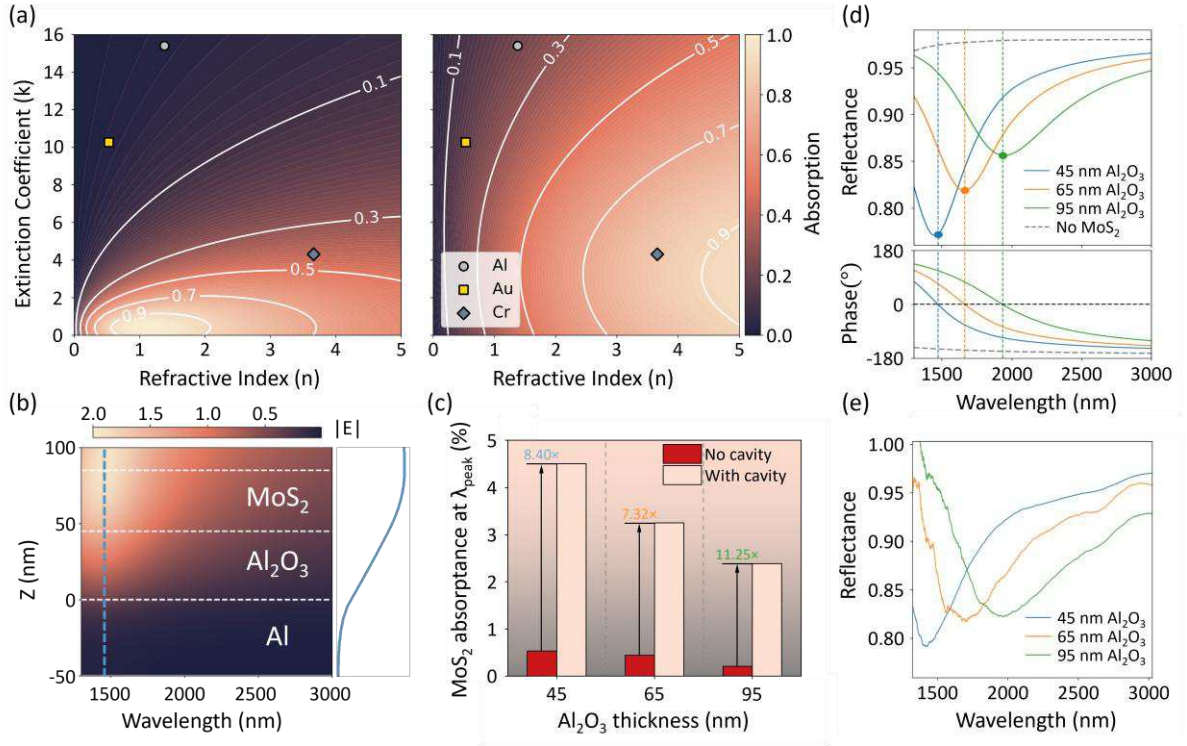


Figure 2. Standing-wave enhancement of MoS_2 target-layer absorption in ultrathin planar cavities. (a) Simulated total absorptance maps as functions of the refractive index and extinction coefficient of the metallic reflector, without (left) and with (right) the MoS_2 target layer; the optical constants of Al, Au and Cr are marked for comparison. (b) Simulated wavelength-dependent electric-field amplitude in the MoS_2/Al_2O_3/Al cavity and the corresponding profile along the z direction at 1470 nm, showing the overlap of the MoS_2 layer with a field antinode. The blue dashed line indicates 1470 nm, and the white dashed lines mark the layer interfaces. (c) Calculated MoS_2 absorptance in cavities with 45-, 65- and 95-nm Al_2O_3 spacers, compared with reference absorptances obtained from measured reflectance and transmittance of the no-cavity MoS_2/quartz structure, assuming negligible absorption in quartz. Each pair is evaluated at the same wavelength, corresponding to the MoS_2 absorption peak in the cavity (λ_{peak}), giving

enhancement factors of 8.40, 7.32 and 11.25, respectively. (d) Calculated reflectance and reflection phase of the complete structures. Colored vertical dashed lines indicate reflection-phase zero crossings, and circles mark the reflectance at those wavelengths. Gray dashed curves show the Al_2O_3/Al reference without MoS_2. (e) Corresponding experimental reflectance spectra measured by FTIR.

2. Ga-Ion Implantation for Controlled Optical-Loss Tuning

To investigate how the optical loss of the target material affects absorption within MoS_2 and its competition with dissipation in the Al reflector, we employ focused ion beam (FIB) Ga-ion implantation as a post-fabrication means of modifying the optical response of MoS_2. Ion irradiation and implantation have been used to modify the defect landscape and physical properties of transition metal dichalcogenides (TMDCs). [19-22] This process introduces Ga atoms together with implantation-induced structural defects into the MoS_2 lattice, as schematically illustrated in Figure 3a. Representative scanning electron microscopy (SEM) images of the implanted MoS_2 regions are shown in Figure 3b. Energy-dispersive X-ray spectroscopy (EDX) was used to quantify the Ga concentration (Supplementary Information Section 6 and Figure S6). Varying the scan-pitch size changes the implantation dose and the resulting EDX-derived Ga concentration, providing a series of samples for investigating the implantation-dependent optical response. Raman measurements reveal redshifts and linewidth broadening of the characteristic MoS_2 modes with increasing Ga concentration, while the Raman peaks remain distinguishable (Figures 3g, h). These changes are consistent with implantation-induced disorder, with possible contributions from local strain and changes in carrier concentration. [23-25] Because Ga incorporation and implantation-induced structural changes occur together, the Raman variations cannot be attributed exclusively to electronic doping.

To further examine a possible microscopic contribution to these implantation-induced changes, we performed density functional theory (DFT) calculations for pristine MoS_2 and an idealized model in which one molybdenum (Mo) atom is replaced by Ga. [26] The model structures and calculated band structures are presented in Supplementary Information Section 7 and Figure S7. Ga substitution introduces additional electronic states near the Fermi level, including partially occupied bands, indicating a modification of the electronic structure in this model. These results identify Ga substitution as a microscopic mechanism capable of modifying the electronic structure of MoS_2, providing a possible contribution to the implantation-induced changes in its optical response. The calculations describe the substitutional-defect contribution, while additional implantation-induced defects may also contribute in the experimental samples.

To connect these material changes with the measured optical response, we first examine how target-layer loss affects cavity reflectance. We calculate the reflectance of the 45- and 95-nm-spacer cavities while varying the MoS_2 extinction coefficient k at a fixed refractive index of n = 4.00 (Figures 3c, d). The independent influence of n is examined in Supplementary Information Section 8 and Figure S8, while the effects of spacer and MoS_2 thickness are examined in Section 9 and Figure S9. Increasing k from the weak-loss regime initially deepens the calculated reflectance minima in both cavity configurations. With negligible transmission, this reduction in reflectance corresponds to increased total absorptance. Experimentally, increasing the implantation dose by reducing the scan-pitch size also lowers the reflectance near the cavity resonance for both spacer thicknesses (Figures 3e, f). The measured trend is qualitatively consistent with the response to increased target-material loss in the parametric

calculations. However, the fixed-n scans do not represent the full optical response of the implanted samples, in which both n and k can change. We therefore focus the subsequent quantitative analysis on the 45-nm-spacer cavities, using dispersive optical constants to calculate the absorptance of each layer and determine how much of the increased total absorptance occurs in MoS_2.

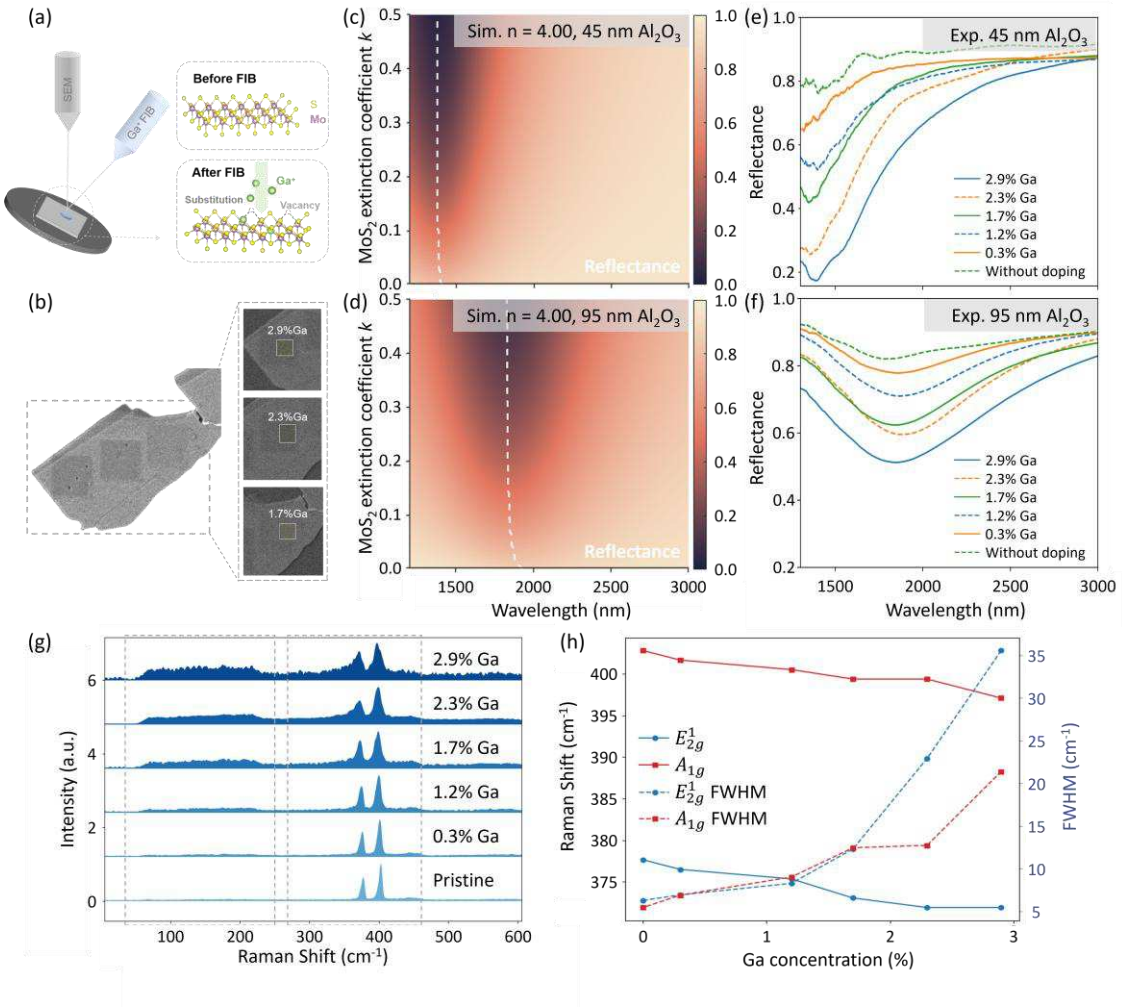


Figure 3. Ga-ion implantation and its effects on the optical response and Raman spectra of $MoS_2/Al_2O_3/Al$ cavities. (a) Schematic of focused ion beam (FIB) implantation, illustrating possible Ga substitution and vacancy formation in MoS_2. (b) Scanning electron microscopy (SEM) images of the MoS_2 flake and selected implanted regions at different Ga concentrations. (c, d) Simulated reflectance maps as functions of wavelength and the MoS_2 extinction coefficient k for cavities with 45- and 95-nm Al_2O_3 spacers, respectively, with the MoS_2 refractive index fixed at n = 4.00. White dashed lines trace the reflectance minima. (e, f) Experimental reflectance spectra of the corresponding cavities at different Ga concentrations. (g) Raman spectra of pristine and Ga-implanted MoS_2, vertically offset for clarity. (h) Peak

positions (solid lines, left axis) and full widths at half maximum (FWHM; dashed lines, right axis) of the E_{2g}^{1} and A_{1g} Raman modes as functions of Ga concentration. Ga concentrations are expressed in atomic percent as determined by energy-dispersive X-ray spectroscopy (EDX).

3. Optical-Loss Enhancement and Layer-Resolved Absorption

The measured reflectance spectra of the 45-nm-spacer cavities were fitted using TMM with a Lorentz-parameterized effective dielectric function whose real and imaginary parts were linked through the Kramers–Kronig (KK) relation. [6,27] The Lorentz terms provide a phenomenological description of material loss and dispersion and are not assigned to specific intrinsic excitonic resonances of MoS_2 in the investigated near-infrared spectral range. For each Ga concentration, the dielectric-function parameters were fitted independently by least-squares minimization of the difference between the measured and calculated reflectance spectra, yielding the effective refractive index n and extinction coefficient k shown in Figures 4a–c. The distinction between the cavity-mode response and the dielectric-function parameterization, together with details of the fitting procedure, is discussed in Supplementary Information Section 10. Within the adopted fitting model, Figures 4b, c show that the fitted effective extinction coefficient k increases systematically with Ga concentration, reaching approximately 0.29 at 1470 nm for the sample with 2.9% Ga, whereas the extracted refractive index n varies more moderately. Through the relation $\alpha(\lambda) = 4\pi k(\lambda)/\lambda$, the fitted increase in k corresponds to a larger material absorption coefficient at a given wavelength. Its effect on absorption within the cavity also depends on the accompanying changes in the internal field. We therefore retain both fitted n and k in the layer-resolved calculations to account for changes in material loss and the electromagnetic response of the complete structure.

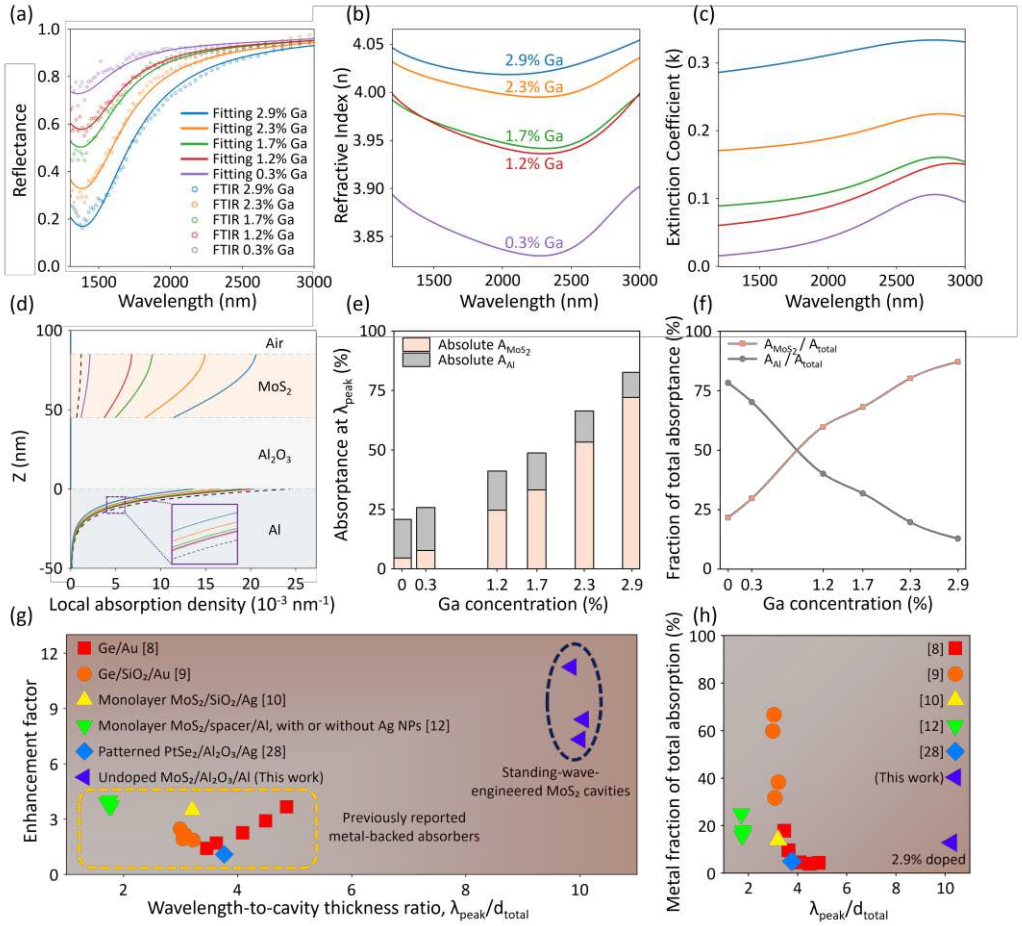


Figure 4. Ga-implantation-dependent optical response, layer-resolved absorption, and benchmarking of MoS_2 planar cavities. (a) Experimental FTIR reflectance spectra (symbols) and corresponding TMM fits obtained using the KK-constrained dielectric-function model (solid lines) for cavities with a 45-nm Al_2O_3 spacer at different EDX-derived Ga concentrations. (b,c) Effective MoS_2 refractive index n and extinction coefficient k extracted from the fits, respectively. (d) Calculated local absorption density at 1470 nm for pristine and Ga-implanted cavities with a 45-nm Al_2O_3 spacer. The absorption density is normalized to the incident intensity, such that its integral over each layer gives that layer's absorptance. Colored curves follow the concentration assignments in (b,c), and the black dashed curve represents pristine MoS_2. Horizontal dashed lines mark the material interfaces. The inset shows an enlarged view of the boxed region within the Al layer to resolve the differences between the absorption-density profiles. (e) Calculated absolute absorptances of the MoS_2 and Al layers and (f) their respective fractions of the total absorptance as functions of Ga concentration for the 45-nm-spacer cavities. Results in (e,f) are evaluated at the MoS_2 absorptance peak wavelength of each sample. (g) Absorption enhancement factor versus wavelength-to-cavity thickness ratio, λ_{peak}/d_{total}, for the pristine cavities in this work and representative metal-backed absorbers. [8-10,12,28] Enhancement factors are defined relative to the respective reference structures. (h) Metal fraction of total absorption, A_{metal}/A_{total}, versus λ_{peak}/d_{total} for benchmark configurations with available layer-resolved absorption data; the result from this work corresponds to the 45-nm-spacer cavity with 2.9% Ga implantation. A_{metal} includes absorption in all metallic components. In (g,h), d_{total} includes the target layer, spacer, metal reflector and any additional structural layers, excluding the substrate. Reference structures, evaluation wavelengths and the sources or recalculation methods for the benchmark

data are specified in the Supplementary Information. Benchmark materials include germanium (Ge), silicon dioxide (SiO_2), silver (Ag) and platinum diselenide ($PtSe_2$); NPs denotes nanoparticles.

Figure 4d compares the calculated local absorption density at a common wavelength of 1470 nm for pristine and Ga-implanted cavities with a 45-nm Al_2O_3 spacer. Normalized to the incident intensity, this quantity is proportional to $\varepsilon''(z)|E(z)/E_{\mathrm{inc}}|^2$, and its integral over each layer gives the corresponding absorptance. Dissipation within MoS_2 increases with Ga concentration despite a reduction in the calculated electric-field amplitude within the target layer, because the increase in the loss weighting, $\varepsilon'' = 2nk$, outweighs the decrease in the layer-integrated field intensity. The corresponding field-intensity profiles and a quantitative comparison of the loss weighting and field-intensity integral are provided in Supplementary Information Section 11 and Figure S10. The accompanying field changes also modify dissipation within the Al reflector. To quantify the absorption partition at peak operation, Figure 4e presents the calculated MoS_2 and Al absorptances evaluated at each sample's MoS_2 absorptance peak wavelength. In the pristine cavity, MoS_2 absorbs approximately 4.50% of the incident power, compared with 16.30% in Al. At 2.9% Ga, the peak MoS_2 absorptance reaches approximately 72.1%, while the Al absorptance at the corresponding wavelength is 10.6%. Consequently, the MoS_2 fraction of total absorption increases from approximately 22% to 87%, as shown in Figure 4f. These results establish a transition from reflector-dominated to target-dominated absorption, accompanied by an increase in total absorptance rather than a simple transfer of a fixed amount of absorbed power between layers. Layer-resolved spectra for the pristine cavities are provided in Supplementary Information Section 12 and Figure S11.

4. Benchmark of Target-Layer Absorption Enhancement, Cavity Compactness, and Energy Dissipation Control

We benchmark the MoS_2 cavities against representative metal-backed absorbers using the target-layer absorption enhancement factor $A^{target}_{with\ cavity}/A^{target}_{no\ cavity}$, the wavelength-to-total-stack-thickness ratio λ_{peak}/d_{total}, and the metal fraction of total absorption A_{metal}/A_{total} (Figure 4g,h). [8-10,12,28] The enhancement factor compares target-layer absorptance with that of the specified reference structure at the same wavelength; its dependence on the reference configuration must therefore be considered when comparing different systems. Since the benchmark structures differ widely in both absolute thickness and operating wavelength, we also use the dimensionless ratio $\lambda_{\mathrm{peak}}/d_{\mathrm{total}}$ as a common measure of the system compactness, where d_{total} includes all constituent layers of the optical stack (including the metal reflector) but excludes the substrate. Larger values correspond to thinner stacks relative to their operating wavelength, with $\lambda_{\mathrm{peak}}/d_{\mathrm{total}} \approx 10$ indicating a total thickness of about $\lambda/10$. Parasitic dissipation is assessed using $A_{\mathrm{metal}}/A_{\mathrm{total}}$, with absorption in all metallic components included in A_{metal}. The same literature set is considered for both comparisons, with the metal-loss comparison restricted to configurations for which layer-resolved absorption can be established. Results from this work correspond to pristine cavities in Figure 4g and the 45-nm-spacer cavity implanted with 2.9% Ga in Figure 4h.

The pristine cavities with 45-, 65-, and 95-nm Al_2O_3 spacers exhibit target-layer absorption enhancement factors of 8.40, 7.32, and 11.25, respectively, with corresponding λ_{peak}/d_{total} of approximately 10.06, 10.01, and 9.85. Figure 4g thus places these cavities in a regime

combining substantial reference-dependent absorption enhancement with total stack thicknesses close to 1/10 of the operating wavelength. The complementary comparison in Figure 4h evaluates parasitic dissipation after optical-loss tuning through Ga implantation. At 2.9% Ga, the Al fraction of total absorption in the 45-nm-spacer cavity is approximately 12.8%, evaluated at its MoS_2 absorptance peak. As a complementary normalization, we also define a normalized absorption-utilization factor $F_{utilize}$, the ratio of the actual target-layer absorptance to the intrinsic single-pass absorptance of the same material at the same wavelength and thickness (see Supplementary Information Section 13). For our pristine MoS_2 cavities, $F_{utilize}$ reaches 11 – 13, indicating that the cavity boosts the ultrathin MoS_2 target-layer absorption to more than ten times its single-pass absorptance.

These results demonstrate that standing-wave-engineered cavities can simultaneously achieve strong target-layer absorption, subwavelength-scale compactness, and efficient redistribution of optical dissipation from the metal reflector into the active material even though some benchmark structures show lower metal fractions. Taken together, the two comparisons separate two distinct quantities: cavity-induced enhancement in pristine MoS_2 (Figure 4g) and the energy dissipation partitioning after optical-loss engineering (Figure 4h). The enhancement factors therefore pertain only to the pristine cavities, not to the implanted samples. Structural parameters, reference configurations, evaluation wavelengths, enhancement factors, and the sources or recalculation methods for the layer-resolved absorption data and metal-loss fractions are provided in Supplementary Information Section 13 and Table S2. As a possible extension, simulations of a cavity with concentric pristine and Ga-implanted regions illustrate

reflective diffractive focusing enabled by spatial patterning of the optical response (Supplementary Information Section 14 and Figure S12).

Conclusion

We establish a standing-wave framework for understanding and controlling the distribution of optical energy dissipation in ultrathin planar cavities. Using $MoS_2/Al_2O_3/Al$ as a model system, layer-resolved electromagnetic analysis shows how cavity phase engineering governs the partitioning of absorbed optical energy between the active material and parasitic metallic losses. By positioning the ultrathin MoS_2 layer near a standing-wave antinode, the cavity strengthens field overlap with a material that is intrinsically weakly absorbing over the investigated near-infrared spectral range and clearly distinguishes target-layer absorption enhancement from suppression of far-field reflectance. For pristine MoS_2, this approach yields calculated absorption enhancement factors of 7.32–11.25 relative to corresponding MoS_2/quartz references at the same wavelengths, with total cavity thicknesses approximately 1/10 of the operating wavelengths. To examine how material loss influences the energy dissipation pathways, we introduce Ga-ion implantation to systematically modify the optical response of MoS_2. Analysis based on optical constants extracted from measured reflectance spectra shows that target-layer absorption can increase even as the internal electric-field amplitude decreases, revealing the coupled influence of material loss and standing-wave field distribution on cavity absorption. In the 45-nm-spacer cavity, the calculated peak MoS_2 absorptance rises from 4.50% in the pristine state to 72.1% at 2.9% Ga concentration, while its share of total absorption increases from approximately 22% to 87%. This transition marks

a reversal of optical energy dissipation, transforming from reflector-dominated to target-dominated absorption, where the majority of absorbed energy is funnelled into the functional ultrathin material. Benchmarking further shows that our maximum enhancement factor exceeds those of the representative absorbers by more than a factor of two, with each enhancement evaluated against its respective reference structure. These findings establish how coordinated control of standing-wave field overlap and target-material loss can redirect optical energy from parasitic metallic dissipation into enhanced absorption in the functional materials for more efficient light–matter interactions in ultrathin photonic devices at telecommunication wavelengths and beyond.

Methodology

Sample Preparation

MoS_2 crystals were purchased from HQ Graphene. A 50-nm Al thin film was deposited on quartz substrates using a Denton Explorer electron-beam evaporator at a rate of 0.5 Å/s, followed by the deposition of Al_2O_3 layers with varying thicknesses using a Beneq TFS 200 atomic layer deposition (ALD) system. The ALD process employed water (H_2O) and trimethylaluminum (TMA, 99.99%) as precursors and was carried out at 120 °C with a purge time of 15 s and a pulse time of 200 ms. All TMDC thin-film samples were prepared by polydimethylsiloxane (PDMS) mechanical exfoliation and viscoelastic stamping transfer. Exfoliation and transfer methods, including emerging approaches toward scalable and automated integration, have been reviewed elsewhere. [29]

Doping was performed using an FEI Helios Nanolab 600 FIB system with Ga^+ ions as the dopant source. The implantation was conducted at an accelerating voltage of 30 kV and a beam current of 10 pA over a 10 μm × 10 μm area. The implantation dose was varied by changing the scan pitch from 90 nm to 10 nm, yielding EDX-derived Ga concentrations ranging from 0.3% to 2.9%.

Characterization Methods

Reflectance measurements were carried out using a Bruker Vertex 80v FTIR spectrometer in reflection mode. A Globar thermal source provided broadband near-infrared illumination, and the signal was collected by a liquid-nitrogen-cooled mercury cadmium telluride (MCT) detector, ensuring high sensitivity and low noise.

EDX was performed on a JEOL JSM-7600F field-emission scanning electron microscope (FESEM) with an accelerating voltage of 10 kV, a probe current of 10 nA, and a working distance of 15 mm.

AFM imaging was conducted on a Bruker Dimension Icon system in tapping mode to obtain the surface morphology of MoS_2, using Bruker standard tapping probes.

Raman spectroscopy was carried out with a WITec Alpha 300R confocal microscope system, employing a 532 nm continuous-wave laser for excitation. The laser beam was focused onto the sample using a 100× objective (numerical aperture, NA = 0.9), and Raman signals were collected through the same objective. A 150 lines/mm diffraction grating was used for spectral

dispersion, and the signals were detected by a thermoelectrically cooled charge-coupled device (CCD).

FDTD Simulation

Numerical simulations of the $MoS_2/Al_2O_3/Al$ structures were performed using the FDTD Solutions software package. Along the z direction, 12-layer perfectly matched layer (PML) boundaries were used to suppress spurious reflections, while periodic boundary conditions were applied in the x and y directions to represent a laterally infinite planar stack. Given the ultrathin thickness of the MoS_2 layer, a fine mesh with a resolution of 0.25 nm was applied along the z-direction in this region to ensure high simulation accuracy and minimize numerical errors.

Transfer Matrix Method and Optical-Constant Fitting

The effective dielectric function of MoS_2 in the Ga-implanted 45-nm-spacer cavities was parameterized using a sum of Lorentz terms, with its real and imaginary parts linked through the KK relation. [6,27] For each Ga concentration, the parameters were fitted independently by least-squares minimization of the difference between the measured reflectance and the full multilayer reflectance calculated using TMM. The MoS_2 thickness was fixed at a nominal value of 40 nm, consistent with the approximately 37-nm thickness measured by AFM for the 45-nm-spacer sample. The optical constants of Al, Al_2O_3 and the quartz substrate were held fixed during fitting and used consistently in the subsequent electromagnetic calculations. Their sources and dispersion assumptions, together with the optical constants used for pristine MoS_2,

are specified in Supplementary Information Section 1. Both the fitted refractive index and extinction coefficient were retained in the subsequent calculations of the internal field and layer-resolved absorption. Layer-resolved absorptance was evaluated using Poynting-flux analysis, as the difference between the net time-averaged power flux entering and leaving each layer, normalized to the incident flux. [15,16,18] For Figure 4d, the air/MoS_2/Al_2O_3/Al/quartz stack was modeled at normal incidence, including the finite 50-nm Al reflector and a semi-infinite quartz substrate. The local absorption density at 1470 nm was calculated as $a(z) = (2\pi/\lambda)\varepsilon''(z)|E(z)/E_{\mathrm{inc}}|^2$, where $\varepsilon''(z)$ is the imaginary part of the relative permittivity of the material at position z. All profiles used the same incident-field normalization. Integration of $a(z)$ over each layer gives its absorptance, normalized to the incident power. For Figures 4e, f, both layer absorptances were evaluated at the MoS_2 absorptance peak wavelength of each sample. Details of the TMM formulation and layer-resolved absorption calculations, optical-constant fitting, and field–loss analysis are provided in Supplementary Information Sections 1, 10, and 11, respectively.

DFT Calculations

DFT calculations were performed using the Fritz Haber Institute ab initio molecular simulations (FHI-aims) package to examine the electronic structure of pristine and Ga-substituted MoS_2. [26] Computational parameters and structural models are described in Supplementary Information Section 7.

Acknowledgements

Z.W. acknowledges financial support from the Young Individual Research Grant (M23M7c0116), administered by the Science and Engineering Research Council (SERC) of the Agency for Science, Technology and Research (A*STAR). J.T. acknowledges financial support from the National Research Foundation, Singapore, under NRF-CRP (NRF-CRP26-2021-0004) and NRFI (NRF-NRFI11-2026-0013). E.J.H.S. acknowledges financial support from the Young Individual Research Grant (Project M23M7c0128). Y.Y. acknowledges the support of the National Natural Science Foundation of China (Grant No. 12604655).

Data Availability

The data supporting the findings of this study are available from the corresponding authors upon reasonable request.

Contributions

Z.W. and J.T. supervised the project. Z.W. and J.L. conceived the idea. J.L. fabricated the samples. J.L., Q.Y.S.W., C.L.L., E.J.H.S., and A.J.S. characterized the samples. J.L., M.S., Y.Y. and H.G. carried out the optical simulations. G.W. carried out the DFT simulations. Y.Y. carried out the TMM-PFA calculations. Z.W., J.T., Y.Y., J.L., H.G., M.S., G.W., Q.Y.S.W., C.L.L. and K.V.S. contributed to the data analysis. J.L., H.G., Y.Y., M.S. and C.L.L. wrote the manuscript. All authors participated in the discussion of the results and the manuscript revision. J.L., H.G., Y.Y., and M.S. contributed equally to this work.

References

1. Mak, K. F. & Shan, J. Photonics and optoelectronics of 2D semiconductor transition metal dichalcogenides. *Nat. Photonics* **10**, 216–226 (2016).
2. Sun, Z., Martinez, A. & Wang, F. Optical modulators with 2D layered materials. *Nat. Photonics* **10**, 227–238 (2016).
3. Liu, C., Guo, J., Yu, L., Li, J., Zhang, M., Li, H., Shi, Y. & Dai, D. Silicon/2D-material photodetectors: from near-infrared to mid-infrared. *Light Sci. Appl.* **10**, 123 (2021).
4. Li, Q., Lu, J., Gupta, P. & Qiu, M. Engineering optical absorption in graphene and other 2D materials: advances and applications. *Adv. Opt. Mater.* **7**, 1900595 (2019).
5. Wang, Z., Sreekanth, K. V., Zhao, M., Nong, J., Liu, Y. & Teng, J. Two-dimensional materials for tunable and nonlinear metaoptics. *Adv. Photonics* **6**, 034001 (2024).
6. Wang, Z., Sebek, M., Liang, X., Elbanna, A., Nemati, A., Zhang, N., Goh, C. H. K., Jiang, M., Pan, J., Shen, Z., Su, X., Thanh, N. T. K., Sun, H. & Teng, J. Greatly enhanced resonant exciton–trion conversion in electrically modulated atomically thin WS_2 at room temperature. *Adv. Mater.* **35**, 2302248 (2023).
7. Elbanna, A., Wang, Z., Liu, Y., Wu, Q. Y. S., Liang, X., Liu, H., Ooi, Z. E., Jiang, M., Deng, J., Sun, H., Pan, J., Shen, Z. & Teng, J. Multi-controllability of ambipolar photoconductivity in transition metal dichalcogenides van der Waals heterostructures. *Adv. Mater. Technol.* **8**, 2301079 (2023).
8. Kats, M. A., Blanchard, R., Genevet, P. & Capasso, F. Nanometre optical coatings based on strong interference effects in highly absorbing media. *Nat. Mater.* **12**, 20–24 (2013).
9. Song, H., Guo, L., Liu, Z., Liu, K., Zeng, X., Ji, D., Zhang, N., Hu, H., Jiang, S. & Gan, Q. Nanocavity enhancement for ultra-thin film optical absorber. *Adv. Mater.* **26**, 2737–2743 (2014).
10. Liu, J.-T., Wang, T.-B., Li, X.-J. & Liu, N.-H. Enhanced absorption of monolayer MoS_2 with resonant back reflector. *J. Appl. Phys.* **115**, 193511 (2014).
11. ElKabbash, M., Letsou, T., Jalil, S. A., Hoffman, N., Zhang, J., Rutledge, J., Lininger, A. R., Fann, C.-H., Hinczewski, M., Strangi, G. & Guo, C. Fano-resonant ultrathin film optical coatings. *Nat. Nanotechnol.* **16**, 440–446 (2021).
12. Bahauddin, S. M., Robatjazi, H. & Thomann, I. Broadband absorption engineering to enhance light absorption in monolayer MoS_2. *ACS Photonics* **3**, 853–862 (2016).
13. Born, M. & Wolf, E. *Principles of Optics: Electromagnetic Theory of Propagation, Inter*ference and Diffraction of Light, 7th expanded edn (Cambridge University Press, 1999).
14. Esfandyarpour, M., Garnett, E. C., Cui, Y., McGehee, M. D. & Brongersma, M. L. Metamaterial mirrors in optoelectronic devices. Nat. Nanotechnol. 9, 542–547 (2014).
15. Byrnes, S. J. Multilayer optical calculations. Preprint at arXiv:1603.02720 (2016).
16. Yang, Y., Agarwal, P., Wang, Z. & Li, Z. Layer-resolved pump absorptance in spintronic/orbitronic terahertz emission modeling: A transfer matrix Poynting flux analysis method with sample-specific parameter fittings. J. Appl. Phys. 140, 063902 (2026).

17. Yang, Y., Dal Forno, S. & Battiato, M. Removal of spectral distortion due to echo for ultrashort THz pulses propagating through multilayer structures with thick substrate. *J. Infrared Millim. Terahertz Waves* **42**, 1142–1152 (2021).
18. Yang, Y., Dal Forno, S. & Battiato, M. Modeling spintronic terahertz emitters as a function of spin generation and diffusion geometry. *Phys. Rev. B* **107**, 144407 (2023).
19. Jadwiszczak, J., Keane, D., Maguire, P., Cullen, C. P., Zhou, Y., Song, H., Downing, C., Fox, D., McEvoy, N., Zhu, R., Xu, J., Duesberg, G. S., Liao, Z.-M., Boland, J. J. & Zhang, H. MoS_2 memtransistors fabricated by localized helium ion beam irradiation. *ACS Nano* **13**, 14262–14273 (2019).
20. Bui, M. N., Rost, S., Auge, M., Tu, J.-S., Zhou, L., Aguilera, I., Blügel, S., Ghorbani-Asl, M., Krasheninnikov, A. V., Hashemi, A., Komsa, H.-P., Jin, L., Kibkalo, L., O'Connell, E. N., Ramasse, Q. M., Bangert, U., Hofsäss, H. C., Grützmacher, D. & Kardynal, B. E. Low-energy Se ion implantation in MoS_2 monolayers. *npj 2D Mater. Appl.* **6**, 42 (2022).
21. Lin, Z., Carvalho, B. R., Kahn, E., Lv, R., Rao, R., Terrones, H., Pimenta, M. A. & Terrones, M. Defect engineering of two-dimensional transition metal dichalcogenides. *2D Mater.* **3**, 022002 (2016).
22. Sarcan, F., Fairbairn, N. J., Zotev, P., Severs-Millard, T., Gillard, D., Wang, X., Conran, B., Heuken, M., Erol, A., Tartakovskii, A. I., Krauss, T. F., Hedley, G. J. & Wang, Y. Understanding the impact of heavy ions and tailoring the optical properties of large-area monolayer WS_2 using focused ion beam. *npj 2D Mater. Appl.* **7**, 23 (2023).
23. Mignuzzi, S., Pollard, A. J., Bonini, N., Brennan, B., Gilmore, I. S., Pimenta, M. A., Richards, D. & Roy, D. Effect of disorder on Raman scattering of single-layer MoS_2. *Phys. Rev. B* **91**, 195411 (2015).
24. Conley, H. J., Wang, B., Ziegler, J. I., Haglund, R. F., Jr., Pantelides, S. T. & Bolotin, K. I. Bandgap engineering of strained monolayer and bilayer MoS_2. *Nano Lett.* **13**, 3626–3630 (2013).
25. Chakraborty, B., Bera, A., Muthu, D. V. S., Bhowmick, S., Waghmare, U. V. & Sood, A. K. Symmetry-dependent phonon renormalization in monolayer MoS_2 transistor. *Phys. Rev. B* **85**, 161403(R) (2012).
26. Blum, V., Gehrke, R., Hanke, F., Havu, P., Havu, V., Ren, X., Reuter, K. & Scheffler, M. Ab initio molecular simulations with numeric atom-centered orbitals. *Comput. Phys. Commun.* **180**, 2175–2196 (2009).
27. Beal, A. R., Liang, W. Y. & Hughes, H. P. Kramers–Kronig analysis of the reflectivity spectra of 3R-WS_2 and 2H-WSe_2. *J. Phys. C: Solid State Phys.* **9**, 2449–2457 (1976).
28. Alfieri, A. D., Motala, M. J., Snure, M., Lynch, J., Kumar, P., Zhang, H., Post, S., Bowen, T., Muratore, C., Robinson, J. A., Hendrickson, J. R., Glavin, N. R. & Jariwala, D. Ultrathin broadband metasurface superabsorbers from a van der Waals semimetal. *Adv. Opt. Mater.* **11**, 2202011 (2023).
29. Ge, H., Liu, J., Sebek, M., Li, Z., Fu, W., Wang, Z. & Wang, Z. AI-assisted wafer-scale exfoliation and transfer of 2D materials: status, challenges and perspectives. *AI for Science* **1**, 013002 (2025).

Supplementary Files

This is a list of supplementary files associated with this preprint. Click to download.

- Supplymentary.docx